

# Phase transitions in the inner crust of neutron stars within the superfluid band theory: Competition between $^1S_0$ pairing and spin polarization under finite temperature and magnetic field

Kenta Yoshimura<sup>1,\*</sup> and Kazuyuki Sekizawa<sup>1,2,3,†</sup>

<sup>1</sup>*Department of Physics, School of Science, Institute of Science Tokyo, Tokyo 152-8551, Japan*

<sup>2</sup>*Nuclear Physics Division, Center for Computational Sciences, University of Tsukuba, Ibaraki 305-8577, Japan*

<sup>3</sup>*RIKEN Nishina Center, Saitama 351-0198, Japan*

(Dated: March 8, 2025)

**Background:** Phase transitions of matter under changes of external environment such as temperature and magnetic field have attracted great interests to various quantum many-body systems. Several phase transitions must have occurred in neutron stars as well such as transitions from normal to superfluid/superconducting phases and crust formation. While the temperature of a proto-neutron star is as high as 10 MeV ( $\approx 10^{11}$  K) or higher, which are above critical temperatures for the emergence of superfluidity and crust formation, it cools rapidly down to 0.1 keV ( $\approx 10^6$  K) already after hundreds of years. While ordinary neutron stars have surface magnetic field strength of around  $10^{12}$  G, those having higher magnetic field strength of  $10^{14-15}$  G or higher, so-called magnetars, have been observed. To uncover detailed evolution of neutron stars from their birth to later years, it is desired to develop fully microscopic approaches that take into account effects of superfluidity/superconductivity, finite temperature and magnetic field, on the same footing.

**Purpose:** The main purpose of this work is twofold: 1) to extend the formalism of the fully self-consistent superfluid nuclear band theory, developed in our previous work [K. Yoshimura and K. Sekizawa, Phys. Rev. C **109**, 065804 (2024)], for finite-temperature and finite-magnetic-field systems; 2) to explore possible phase transitions of nuclear matter by varying temperature and magnetic field.

**Methods:** We employ the superfluid band theory which is based on the Kohn-Sham density functional theory (DFT) for superfluid systems with a local treatment of pairing, known as superfluid local density approximation (SLDA), subjected to the Bloch boundary conditions. We assume periodic spatial variation along  $z$ -direction with uniform distribution along  $xy$ -direction, allowing us to describe the slab phase as well as uniform nuclear matter. The finite-temperature extension is achieved in a similar manner as a finite-temperature Hartree-Fock-Bogoliubov calculation. Magnetic field effects are introduced taking into account both the Landau levels formation of relativistic electrons and the couplings of the magnetic field with nucleons' magnetic moments.

**Results:** We have performed superfluid band theory calculations for the slab phase of neutron star matter at  $n_B = 0.04, 0.05, 0.06,$  and  $0.07 \text{ fm}^{-3}$  under various sets of temperature and magnetic field. From the results without magnetic field ( $B = 0$ ), we find that the superfluidity of neutrons disappears at around  $k_B T = 0.6\text{--}0.9 \text{ MeV}$ , and “melting” of nuclear slabs, that is, a structural change into the uniform matter, takes place at around  $k_B T = 2.5\text{--}4.5 \text{ MeV}$ . By turning on the magnetic field, we find that protons' spin gets polarized at around  $B = 10^{16}$  G, whereas neutrons' spin is kept unpolarized on average up to around  $B = 10^{17}$  G. Intriguingly, our microscopic calculations reveal that neutrons' spin is actually polarized *locally* inside and outside of the slab already at  $B \sim 10^{16}$  G, while keeping the system unpolarized in total. We show that the local polarization of neutrons' spin is caused by an interplay of  $^1S_0$  pairing among neutrons and spin-dependent interactions between neutron and protons.

**Conclusions:** We have demonstrated validity and usefulness of the fully self-consistent superfluid nuclear band theory for describing neutron star matter under arbitrary temperature and magnetic field. Critical temperatures and magnetic fields have been predicted for 1) superfluid to normal transition, 2) crust formation, and 3) spin polarization, under conditions relevant to realistic neutron star environments.

## I. INTRODUCTION

How has each of neutron stars evolved from its birth to the present day? To answer this question, one must know details of the states of nuclear matter under arbitrary temperature and magnetic field. Among the theoretical models on the market, the nuclear density functional theory (DFT) [1–4], also regarded as the (relativistic and non-relativistic) mean-field theory [5], is a microscopic approach for describing nuclear matter properties as many-nucleon systems. There have been both static [6–9] and dynamic [10–12] mean-field calculations for complex crystalline structures in the inner crust, which are

known as the pasta phases. The most sophisticated description of the pasta phases to date is realized by the self-consistent band theory based on nuclear DFT, which was first achieved for the slab phase [13] and was later extended to describe time-dependent [14] and superfluid [15, 16] phenomena, as well as the rod phase [17]. However, the applications of the (time-dependent) superfluid band theory have so far been limited to zero temperature without magnetic field. Although it is, of course, sufficient to investigate structures of cold, ordinary neutron stars, it is insufficient to uncover the evolution from supernova matter through a hot proto-neutron star to a cold one. This article aims to establish the theoretical framework of the superfluid band theory at finite temperature and magnetic field. As a first step, we apply it to the slab and uniform phase of neutron star matter to demonstrate its feasibility.

The nuclear band theory may not yet be a widely known

\* yoshimura.k.af21@m.isct.ac.jp

† sekizawa@phys.sci.isct.ac.jp

concept in the nuclear physics community. The band theory of solids [18], which is at the heart of solid-state physics, takes proper account of a periodic potential in quantum mechanical theories in terms of the Bloch boundary conditions. Because in the inner crust of neutron stars dripped free neutrons permeate the crystalline structure of nuclear matter, one has to use the band theory of solids to quantify the effects of periodic structure on dripped, superfluid neutrons. The first realistic calculations on band structure effects in the inner crust of neutron stars were reported in 2005 for slab and rod phases [19] and Coulomb lattices of spherical nuclei [20]. Notably, it was shown [20–22] that the band structure effects, which are caused by the Bragg scatterings of dripped neutrons off the periodic potential, may significantly reduce the superfluid fraction, leading to a crisis [23, 24] for the models of pulsar glitches [25]. The latter effect has been called the “entrainment effects.” To provide a conclusive understanding of the entrainment phenomenon, fully self-consistent band theories based on nuclear DFT have been developed. The self-consistent nuclear band theory was first achieved for the slab phase neglecting pairing correlations [13], which was later extended for time-dependent problems [14], where both calculations indicate that the band structure affects in an opposite way for the slab phase, which is called the “anti-entrainment effect.” Recently, we have extended the theoretical framework of the nuclear band theory to describe neutron superfluidity and proton superconductivity in a fully self-consistent manner [15], showing that the anti-entrainment effect is present in the slab phase even with the inclusion of neutron superfluidity.

By further extending the theoretical framework for systems with finite temperature and magnetic field, we can establish a fully self-consistent microscopic theory for neutron star matter, which can be applied from crust to the outer core, under arbitrary environment. Of course, to describe the formation process of a neutron star, one must rely on elaborated simulation codes of supernova explosions demanding microscopic input. We aim to provide reliable microscopic information of the state of nuclear matter under a wide range of extreme conditions that are realized in the explosive situations.

Concerning the finite-temperature effects, temperature reaches as high as 10 MeV or higher during and just after a supernova explosion, which is enough to alter nuclear matter properties; *e.g.*, neutron superfluidity would disappear at temperature around 1 MeV, and the crust is expected to “melt” to form uniform nuclear matter at several MeV. The change in shapes and compositions of the pasta structure affects neutrino scattering cross sections and thus opacity for neutrino flux [9], as well as the cooling processes [26]. For example, the band structure effects alter the effective mass of free neutrons, which leads to the change of heat conduction [21, 27]. In addition, the neutron superfluidity may not only reduce the neutrino emissivity [28, 29], but also initiate another contribution to neutrino emissions from the so-called pair breaking and formation (PBF) processes [30–33], whose temperature and structure dependence should be quantitatively examined.

On the other hand, strong magnetic field of neutron stars may affect nuclear matter properties through magnetic interactions with neutrons and protons as well as electrons. The re-

cent observations of magnetars [34–37] indicate strong magnetic fields on the order of  $10^{14-15}$  G or higher. Such a strong magnetic field leads to a discretization of electron energy spectra, known as the Landau-Rabi quantization. This quantum mechanical effect alters the equation of state (EoS) of the crustal matter as well as the composition of nuclei in the outer crust [21, 38–41]. Some theoretical calculations showed that magnetic field can be even stronger, at least locally as large as  $10^{17}$  G, *e.g.* in a form of a toroidal magnetic field [42–44]. When the magnetic field strength exceeds  $10^{17}$  G, the shifts of single-particle energies of neutrons and protons become on the order of MeV, and quantum shells and level ordering and, as a consequence, deformation of nuclear clusters, can be affected [38, 39, 45, 46]. Furthermore, it has been advocated that superheavy nuclei, including unknown elements, may emerge as a stable, equilibrium configuration of the outer crust under a superstrong magnetic field as strong as  $10^{18}$  G [41, 47].

We point out here that interplay between pairing correlations and spin polarization in the presence of magnetic field is intriguing and important. A superstrong magnetic field stronger than  $B \sim 10^{17}$  G can, on one hand, break spin-singlet Cooper pairs, but on the other hand, may assist formation of spin-triplet Cooper pairs (see, *e.g.*, Ref. [48]), which may alter thermal conductivity and cooling rate. When a magnetic field breaks Cooper pairs, neutrons and protons may cause spin polarization. It has been shown that the interplay between spin polarization and pairing correlations could manifest a unique pairing phase, known as the Larkin-Ovchinnikov-Fulde-Ferrell (LOFF) phase [49–51]. Recently, effects of spin polarization in strongly correlated Fermionic systems, known as unitary Fermi gas, have been explored within superfluid (TD)DFT, predicting possible existence of a spin-polarized droplet, dubbed as “ferron” [52, 53], and of complex spin-polarized structural patterns [54]. Moreover, spatial modulation of spin orientations can form topological objects such as Skyrmions [55–57]. A fully microscopic investigation of such exotic phases in nuclear matter has not yet been achieved to date, and this work is positioned as a first step towards exploring the above mentioned exotic possibilities in the nuclear physics context.

In the present paper, we extend the theoretical framework of the self-consistent superfluid band theory [15] for finite-temperature and finite-magnetic-field systems. The theory is based on Kohn-Sham DFT and its superfluid extension with a local treatment of pairing, known as superfluid local density approximation (SLDA) [58–60]. The finite-temperature extension is achieved in the same manner as in finite-temperature Hartree-Fock-Bogoliubov calculations [61, 62]. The magnetic field effects are incorporated in both the magnetic interaction acting on the magnetic moments of neutrons and protons (see, *e.g.*, Refs. [45, 46]) as well as the formation of the Landau levels of relativistic electrons (see, *e.g.*, Ref. [21]). By applying the extended framework to the slab phase of neutron star matter, we explore the states of nuclear matter under various sets of temperature and magnetic fields. Intriguingly, we find nontrivial local polarizations of neutrons’ spin at  $B \simeq 10^{16}$  G, which is caused by an interplay

between  $^1S_0$  pairing correlations among neutrons and spin-dependent interactions between neutrons and protons.

The article is organized as follows. In Sec. II A, the theoretical framework of the fully self-consistent superfluid band theory is described, especially focusing on the extensions to finite-temperature and finite-magnetic-field systems. In Sec. III, the results of numerical calculations are presented, showing how nuclear matter properties are altered with varying temperature and magnetic field. A summary and a future prospect are given in Sec. IV.

## II. FORMULATION

### A. Self-consistent nuclear band theory for superfluid systems

In this section, we provide the formulation of the fully self-consistent band theory based on nuclear DFT for superfluid systems. The fully self-consistent band theory was first achieved for the slab phase in 2019 [13], which was extended for time-dependent phenomena in 2022 [14]. To take into account neutron superfluidity, we have recently extended [15] the theoretical framework based on a superfluid DFT, known as SLDA.

Here we recall the formalism of the superfluid band theory, introducing various notations. Let us consider a generic Hamiltonian in the second-quantized form,

$$\hat{H} = \sum_{ij} t_{ij} \hat{a}_i^\dagger \hat{a}_j + \sum_{ijkl} \bar{v}_{ijkl} \hat{a}_i^\dagger \hat{a}_j^\dagger \hat{a}_l \hat{a}_k, \quad (1)$$

where  $\hat{a}_i^\dagger$  ( $\hat{a}_i$ ) represents the particle creation (annihilation) operator for an  $i$ th quantum state,  $t_{ij}$  and  $\bar{v}_{ijkl} = v_{ijkl} - v_{ijlk}$  are matrix elements of kinetic and interaction operators, respectively. For the creation and annihilation operators, we introduce the Bogoliubov transformation,

$$\begin{pmatrix} \hat{\beta} \\ \hat{\beta}^\dagger \end{pmatrix} = \mathcal{W}^\dagger \begin{pmatrix} \hat{a} \\ \hat{a}^\dagger \end{pmatrix}, \quad (2)$$

where  $\hat{\beta} = (\hat{\beta}_1, \hat{\beta}_2, \dots)^\top$  and  $\hat{\beta}^\dagger = (\hat{\beta}_1^\dagger, \hat{\beta}_2^\dagger, \dots)^\top$  ( $\top$  stands for a ‘transpose’ operation and similar definitions apply for  $\hat{a}$  and  $\hat{a}^\dagger$ ). The Bogoliubov transformation matrix,

$$\mathcal{W} = \begin{pmatrix} U & V^* \\ V & U^* \end{pmatrix}, \quad (3)$$

defines the quasiparticle creation and annihilation operators,  $\hat{\beta}_\mu^\dagger$  and  $\hat{\beta}_\mu$ . Based on the variational principle for the HFB state being quasiparticle vacuum, one obtains the HFB equation,

$$\begin{pmatrix} h - \lambda I & \Delta \\ -\Delta^* & -h^* + \lambda I \end{pmatrix} \begin{pmatrix} U_\mu \\ V_\mu \end{pmatrix} = E_\mu \begin{pmatrix} U_\mu \\ V_\mu \end{pmatrix}, \quad (4)$$

where  $U_\mu$  and  $V_\mu$  represent the  $\mu$ th column of matrices  $U$  and  $V$ , respectively, and  $E_\mu$  denotes the corresponding quasiparticle energy.  $h = t + \Gamma$  is the single-particle Hamiltonian matrix with a matrix of the mean-field potential  $\Gamma$ , and that of the pairing potential  $\Delta$ . The latter two potential matrices contain the matrix elements which are defined by

$$\Gamma_{kl} = \sum_{mn} \bar{v}_{kmln} \rho_{nm}, \quad (5)$$

$$\Delta_{kl} = \frac{1}{2} \sum_{mn} \bar{v}_{klmn} \kappa_{mn}, \quad (6)$$

with the density matrix and the pairing tensor,

$$\rho_{kl} = \langle \hat{a}_l^\dagger \hat{a}_k \rangle = (V^* V^\top)_{kl} \quad (7)$$

$$\kappa_{kl} = \langle \hat{a}_l \hat{a}_k \rangle = (V^* U^\top)_{kl}. \quad (8)$$

Writing down explicitly spin ( $\sigma = \uparrow, \downarrow$ ) and isospin ( $q = n, p$ ) degrees of freedom, the coordinate-space representation of the HFB equation is given by

$$\begin{pmatrix} \hat{h}_{\uparrow\uparrow}^{(q)}(\mathbf{r}) - \lambda & \hat{h}_{\uparrow\downarrow}^{(q)}(\mathbf{r}) & 0 & \Delta(\mathbf{r}) \\ \hat{h}_{\downarrow\uparrow}^{(q)}(\mathbf{r}) & \hat{h}_{\downarrow\downarrow}^{(q)}(\mathbf{r}) - \lambda & -\Delta(\mathbf{r}) & 0 \\ 0 & -\Delta^*(\mathbf{r}) & -\hat{h}_{\uparrow\uparrow}^{(q)*}(\mathbf{r}) + \lambda & -\hat{h}_{\uparrow\downarrow}^{(q)*}(\mathbf{r}) \\ \Delta^*(\mathbf{r}) & 0 & -\hat{h}_{\downarrow\uparrow}^{(q)*}(\mathbf{r}) & -\hat{h}_{\downarrow\downarrow}^{(q)*}(\mathbf{r}) + \lambda \end{pmatrix} \begin{pmatrix} u_\mu^{(q)}(\mathbf{r}\uparrow) \\ u_\mu^{(q)}(\mathbf{r}\downarrow) \\ v_\mu^{(q)}(\mathbf{r}\uparrow) \\ v_\mu^{(q)}(\mathbf{r}\downarrow) \end{pmatrix} = E_\mu^{(q)} \begin{pmatrix} u_\mu^{(q)}(\mathbf{r}\uparrow) \\ u_\mu^{(q)}(\mathbf{r}\downarrow) \\ v_\mu^{(q)}(\mathbf{r}\uparrow) \\ v_\mu^{(q)}(\mathbf{r}\downarrow) \end{pmatrix}, \quad (9)$$

where we consider the spin-singlet pairing,  $\Delta(\mathbf{r}) \equiv \Delta_{\uparrow\downarrow}(\mathbf{r}) = -\Delta_{\downarrow\uparrow}(\mathbf{r})$ . We call  $u_\mu^{(q)}(\mathbf{r}\sigma)$  and  $v_\mu^{(q)}(\mathbf{r}\sigma)$  the quasiparticle wave functions.

In the superfluid band theory, we impose the Bloch bound-

ary condition to the quasiparticle wave functions:

$$u_{\mu\mathbf{k}}^{(q)}(\mathbf{r}\sigma) = \frac{1}{\sqrt{\mathcal{V}}} \tilde{u}_{\mu\mathbf{k}}^{(q)}(\mathbf{r}\sigma) e^{i\mathbf{k}\cdot\mathbf{r}} \quad (10)$$

$$v_{\mu\mathbf{k}}^{(q)}(\mathbf{r}\sigma) = \frac{1}{\sqrt{\mathcal{V}}} \tilde{v}_{\mu\mathbf{k}}^{(q)}(\mathbf{r}\sigma) e^{i\mathbf{k}\cdot\mathbf{r}}, \quad (11)$$

where  $\mathcal{V}$  is a normalization volume. The indexes  $\mu$  and  $\mathbf{k}$  are referred to as a band index and a Bloch wave number, re-

spectively. The above definitions are consistent with imposing the Bloch boundary condition to the single-particle wave functions [15]. We can derive the HFB equation for the di-

mensionless functions,  $\tilde{u}_{\mu\mathbf{k}}^{(q)}(\mathbf{r}\sigma)$  and  $\tilde{v}_{\mu\mathbf{k}}^{(q)}(\mathbf{r}\sigma)$  [15], and the resulting equations read:

$$\begin{pmatrix} \hat{h}_{\uparrow\uparrow}^{(q)} + \hat{h}_{\mathbf{k},\uparrow\uparrow}^{(q)} - \lambda & \hat{h}_{\downarrow\downarrow}^{(q)} + \hat{h}_{\mathbf{k},\uparrow\downarrow}^{(q)} & 0 & \Delta_q \\ \hat{h}_{\downarrow\uparrow}^{(q)} + \hat{h}_{\mathbf{k},\uparrow\downarrow}^{(q)} & \hat{h}_{\downarrow\downarrow}^{(q)} + \hat{h}_{\mathbf{k},\downarrow\downarrow}^{(q)} - \lambda & -\Delta_q & 0 \\ 0 & -\Delta_q^* & -\hat{h}_{\uparrow\uparrow}^{(q)*} - \hat{h}_{-\mathbf{k},\uparrow\uparrow}^{(q)*} + \lambda & -\hat{h}_{\downarrow\downarrow}^{(q)*} - \hat{h}_{-\mathbf{k},\uparrow\downarrow}^{(q)*} \\ \Delta_q^* & 0 & -\hat{h}_{\uparrow\uparrow}^{(q)*} - \hat{h}_{-\mathbf{k},\uparrow\downarrow}^{(q)*} & -\hat{h}_{\downarrow\downarrow}^{(q)*} - \hat{h}_{-\mathbf{k},\downarrow\downarrow}^{(q)*} + \lambda \end{pmatrix} \begin{pmatrix} \tilde{u}_{\mu\mathbf{k}}^{(q)}(\mathbf{r}\uparrow) \\ \tilde{u}_{\mu\mathbf{k}}^{(q)}(\mathbf{r}\downarrow) \\ \tilde{v}_{\mu\mathbf{k}}^{(q)}(\mathbf{r}\uparrow) \\ \tilde{v}_{\mu\mathbf{k}}^{(q)}(\mathbf{r}\downarrow) \end{pmatrix} = E_{\mu\mathbf{k}}^{(q)} \begin{pmatrix} \tilde{u}_{\mu\mathbf{k}}^{(q)}(\mathbf{r}\uparrow) \\ \tilde{u}_{\mu\mathbf{k}}^{(q)}(\mathbf{r}\downarrow) \\ \tilde{v}_{\mu\mathbf{k}}^{(q)}(\mathbf{r}\uparrow) \\ \tilde{v}_{\mu\mathbf{k}}^{(q)}(\mathbf{r}\downarrow) \end{pmatrix}. \quad (12)$$

Here we omit the coordinate index ( $\mathbf{r}$ ) in the HFB matrix for a concise expression. The single-particle Hamiltonian with the Bloch wave number  $\hat{h}_{\mathbf{k},\sigma\sigma'}$  can be formally obtained by the following replacement of the derivative operator in  $\hat{h}_{\sigma\sigma'}$ :

$$\nabla \rightarrow \nabla + i\mathbf{k}. \quad (13)$$

For more detailed description, we refer readers to Refs. [14, 15].

## B. Energy density functional

For practical applications, we employ nuclear energy density functional (EDF) approach. In the present work, we use a Skyrme-type EDF, as in our previous work [15]. We work with the nuclear EDF of the following form:

$$\frac{E_{\text{nucl}}}{A} = \frac{1}{N_b} \int (\mathcal{E}_{\text{kin}}(\mathbf{r}) + \mathcal{E}_{\text{Sky}}(\mathbf{r}) + \mathcal{E}_{\text{Coul}}^{(p)}(\mathbf{r}) + \mathcal{E}_{\text{pair}}(\mathbf{r})) d\mathbf{r}. \quad (14)$$

The kinetic energy part,  $\mathcal{E}_{\text{kin}}$ , the nuclear interaction part,  $\mathcal{E}_{\text{Sky}}$ , the Coulomb part,  $\mathcal{E}_{\text{Coul}}$ , and the pairing part,  $\mathcal{E}_{\text{pair}}(\mathbf{r})$ , in the nuclear EDF are given, respectively, by

$$\mathcal{E}_{\text{kin}}(\mathbf{r}) = \sum_{q=n,p} \frac{\hbar^2}{2m_q} \tau_q(\mathbf{r}), \quad (15)$$

$$\begin{aligned} \mathcal{E}_{\text{Sky}}(\mathbf{r}) = & \sum_{t=0,1} \left[ C_t^p [n_0] n_t^2(\mathbf{r}) + C_t^{\Delta\rho} n_t(\mathbf{r}) \partial_z^2 n_t(\mathbf{r}) \right. \\ & + C_t^\tau (n_t(\mathbf{r}) \tau_t(\mathbf{r}) - \mathbf{j}_t^2(\mathbf{r})) \\ & + C_t^s [n_0] s_t^2(\mathbf{r}) + C_t^{\Delta s} s_t(\mathbf{r}) \cdot \Delta s_t(\mathbf{r}) \\ & \left. + C_t^T (s_t(\mathbf{r}) \cdot \mathbf{T}_t(\mathbf{r}) - J_t^2(\mathbf{r})) \right], \quad (16) \end{aligned}$$

$$\mathcal{E}_{\text{Coul}}^{(p)}(\mathbf{r}) = \frac{1}{2} V_{\text{Coul}}(\mathbf{r}) n_p(\mathbf{r}) - \frac{3e^2}{4} \left( \frac{3}{\pi} \right)^{1/3} n_p^{4/3}(\mathbf{r}), \quad (17)$$

$$\mathcal{E}_{\text{pair}}(\mathbf{r}) = - \sum_{q=n,p} \Delta_q(\mathbf{r}) \kappa_q^*(\mathbf{r}), \quad (18)$$

where  $\hbar$  is the reduced Plank's constant,  $m_q$  denotes the mass of a neutron ( $q = n$ ) and a proton ( $q = p$ ), and  $e$  is the elementary charge.  $n$ ,  $\tau$ ,  $\mathbf{j}$ ,  $\mathbf{s}$ ,  $\mathbf{T}$ , and  $J$  are various nucleonic densities, whose explicit definitions will be given later. The

index  $t$  represents isoscalar ( $t = 0$ , e.g.  $n_0 = n_n + n_p$ ) and isovector ( $t = 1$ , e.g.  $n_1 = n_n - n_p$ ) components.  $C_t^X$  ( $X = \rho, \Delta\rho, \dots$ ) are the parameters of the functional, which are determined to reproduce the known properties of finite nuclei and nuclear matter. In the functional shown above, the spin-orbit term is omitted, because it does not play any role in the systems with spatial modulations along a certain single dimension, like a slab phase. In the present work, we include time-odd components in the functional, as the external magnetic field breaks the time-reversal symmetry. Note, however, that since the  $\mathbf{s} \cdot \Delta \mathbf{s}$  term is known to cause a spin instability, we set  $C_t^{\Delta s} = 0$  throughout our analysis.

For the electron part, we adopt an EDF for relativistic electron gas,

$$\frac{E_{\text{elec}}}{A} = \frac{1}{N_b} (\mathcal{E}_{\text{kin}}^{(e)} + \mathcal{E}_{\text{Coul}}^{(e)}) a, \quad (19)$$

where

$$\begin{aligned} \mathcal{E}_{\text{elec}} &= \int_0^{p_F} \frac{4\pi p^2 dp}{(2\pi)^3} \sqrt{m_e^2 c^4 + p^2 c^2} \\ &= \frac{m_e^4 c^5}{32\pi^2 \hbar^3} (\sinh \theta_F - 4\theta_F), \quad (20) \end{aligned}$$

$$\mathcal{E}_{\text{Coul}}^{(e)} = -\frac{3e^2}{4} \left( \frac{3}{\pi} \right)^{1/3} n_e^{4/3}, \quad (21)$$

where  $p_F = \hbar(3\pi^2 n_e)^{1/3}$  denotes the Fermi momentum with the electron number density  $n_e$ .  $\theta_F$  is defined through the relation,  $\varepsilon_e = \sqrt{m^2 c^4 + p_F^2 c^2} = m_e c^2 \cosh \theta_F$ . The Coulomb exchange term is evaluated with the Slater approximation, while the direct term of the electrons' Coulomb energy vanishes because of the charge neutrality condition. It is to mention here that the electronic EDF will be modified in the presence of an external magnetic field, which will be discussed in Sec. II D.

From appropriate functional derivatives, one can derive the ordinary ( $\mathbf{k}$ -independent) single-particle Hamiltonian,

$$\begin{aligned} \hat{h}_{\sigma\sigma'}^{(q)}(\mathbf{r}) = & -\nabla \cdot M^{(q)}(\mathbf{r}) \nabla + U^{(q)}(\mathbf{r}) \\ & + \Sigma^{(q)}(\mathbf{r}) \cdot \boldsymbol{\sigma} + \frac{1}{2i} \left[ \nabla \cdot \mathbf{I}^{(q)}(\mathbf{r}) + \mathbf{I}^{(q)}(\mathbf{r}) \cdot \nabla \right], \quad (22) \end{aligned}$$

as well as the  $\mathbf{k}$ -dependent one,

$$\hat{h}_{\mathbf{k}}^{(q)}(\mathbf{r}) = M^{(q)}(\mathbf{r}) \mathbf{k}^2 + \hbar \mathbf{k} \cdot \hat{\mathbf{v}}^{(q)}(\mathbf{r}), \quad (23)$$

where

$$\begin{aligned}\hat{v}^{(q)}(\mathbf{r}) &= \frac{1}{i\hbar} \left[ \mathbf{r}, \hat{h}^{(q)}(\mathbf{r}) \right] \\ &= -i\hbar \left[ \nabla M^{(q)}(\mathbf{r}) + M^{(q)}(\mathbf{r}) \nabla \right] + \frac{1}{\hbar} \mathbf{I}^{(q)}(\mathbf{r}).\end{aligned}\quad (24)$$

The various mean-field potentials in the single-particle Hamiltonian are defined as follows:

$$\begin{aligned}M^{(q)}(\mathbf{r}) &= \frac{\hbar^2}{2m_q} + \sum_{q'=n,p} C_{q'}^{\tau(q)} n_{q'}(\mathbf{r}), \\ &+ \sum_{q'=n,p} C_{q'}^{\mathbf{T}(q)} \boldsymbol{\sigma} \cdot \mathbf{s}_{q'}(\mathbf{r})\end{aligned}\quad (25)$$

$$\begin{aligned}U^{(q)}(\mathbf{r}) &= \sum_{q'=n,p} \left[ 2C_{q'}^{\rho(q)} n_{q'}(\mathbf{r}) + 2C_{q'}^{\nabla\rho(q)} \partial_z^2 n_{q'}(\mathbf{r}) \right. \\ &+ \left. C_{q'}^{\tau(q)} \tau_{q'}(\mathbf{r}) + 2n_0^\alpha(\mathbf{r}) C_{q'D}^{\rho(q)} n_{q'}(\mathbf{r}) \right] \\ &+ \alpha n_0^{\alpha-1}(\mathbf{r}) \sum_{t=0,1} C_t^\rho [n_0] n_t^2(\mathbf{r}) \\ &+ U_{\text{Coul}}(\mathbf{r}) \delta_{qp} + \sum_{q'=n,p} \frac{\partial g_{q',\text{eff}}}{\partial n_q} |\kappa_{q'}(\mathbf{r})|^2,\end{aligned}\quad (26)$$

$$\Sigma^{(q)}(\mathbf{r}) = \sum_{q'=n,p} \left[ 2C_{q'}^{\mathbf{s}(q)} [n_0] \mathbf{s}_{q'}(\mathbf{r}) + C_{q'}^{\mathbf{T}(q)} [n_0] \mathbf{T}_{q'}(\mathbf{r}) \right],\quad (27)$$

$$\mathbf{I}^{(q)}(\mathbf{r}) = -2 \sum_{q'=n,p} C_{q'}^{\tau(q)} \mathbf{j}_{q'}(\mathbf{r}).\quad (28)$$

In the above formulas, the coefficients with two isospin indices  $C_{q'}^{\mathbf{X}(q)}$  are the shorthand notations, defined by:

$$C_n^{\mathbf{X}(q)} \equiv C_0^{\mathbf{X}} + \eta_q C_1^{\mathbf{X}},\quad (29)$$

$$C_p^{\mathbf{X}(q)} \equiv C_0^{\mathbf{X}} - \eta_q C_1^{\mathbf{X}},\quad (30)$$

where X stands for the superscript of the coefficients, *e.g.*,  $\rho$ ,  $\tau$ , etc., and  $\eta_q = +1$  ( $-1$ ) for neutrons (protons).

In the SLDA formalism, the pairing field  $\Delta_q(\mathbf{r})$  is local in space:

$$\Delta_q(\mathbf{r}) = -g_{q,\text{eff}}(\mathbf{r}) \kappa_q(\mathbf{r}).\quad (31)$$

Here,  $g_{q,\text{eff}}$  is an effective pairing coupling constant [58] calculated as [60]

$$\frac{1}{g_{q,\text{eff}}} = \frac{1}{g_0} - \frac{K}{8\pi^2 M^{(q)}} \frac{\pi}{\Delta z},\quad (32)$$

where  $g_0$  denotes the bare coupling constant,  $K$  is a numerical constant [60], and  $\Delta z$  is the spatial mesh spacing. The anomalous density is defined by

$$\kappa_q(\mathbf{r}) = \sum_{\mu\mathbf{k}} v_{\mu\mathbf{k}\uparrow}^{(q)*}(\mathbf{r}\sigma) u_{\mu\mathbf{k}\downarrow}^{(q)}(\mathbf{r}\sigma).\quad (33)$$

We note that there is an additional contribution to  $U^{(q)}(\mathbf{r})$  arising from the density dependence of the effective pairing coupling constant, which is given by

$$\frac{\partial g_{q',\text{eff}}}{\partial n_q} = [g_{q',\text{eff}}(\mathbf{r})]^2 \frac{K}{8\pi^2 \Delta z} \left( M^{(q')}(\mathbf{r}) \right)^{-2} C_{q'}^{\tau(q')}. \quad (34)$$

The single-particle Hamiltonian are given as a functional of various densities. Those densities are given in terms of the quasiparticle wave functions as follows:

$$n_q(\mathbf{r}) = \sum_{\mu\mathbf{k}\sigma} \left| v_{\mu\mathbf{k}}^{(q)}(\mathbf{r}\sigma) \right|^2,\quad (35)$$

$$\tau_q(\mathbf{r}) = \sum_{\mu\mathbf{k}\sigma} \left| \nabla v_{\mu\mathbf{k}}^{(q)}(\mathbf{r}\sigma) \right|^2,\quad (36)$$

$$\mathbf{j}_q(\mathbf{r}) = -\sum_{\mu\mathbf{k}\sigma} \text{Im} \left[ v_{\mu\mathbf{k}}^{(q)*}(\mathbf{r}\sigma) \nabla v_{\mu\mathbf{k}}(\mathbf{r}\sigma) \right],\quad (37)$$

$$\mathbf{s}_q(\mathbf{r}) = \sum_{\mu\mathbf{k}ss'} v_{\mu\mathbf{k}}^{*(q)}(\mathbf{r}s) v_{\mu\mathbf{k}}^{(q)}(\mathbf{r}s') \boldsymbol{\sigma}_{ss'},\quad (38)$$

$$\mathbf{T}_q(\mathbf{r}) = \sum_{\mu\mathbf{k}ss'} \left[ \nabla v_{\mu\sigma}^{*(q)}(\mathbf{r}s) \cdot \nabla v_{\mu\sigma}^{(q)}(\mathbf{r}s') \right] \boldsymbol{\sigma}_{ss'},\quad (39)$$

$$\begin{aligned}J_{q,\alpha\beta}(\mathbf{r}) &= -\frac{1}{2i} \sum_{\mu\mathbf{k}ss'} \left[ v_{\mu\mathbf{k}}^{*(q)}(\mathbf{r}s') (\nabla_\alpha v_{\mu\mathbf{k}}(\mathbf{r}s)) \right. \\ &\quad \left. - v_{\mu\mathbf{k}}^{(q)}(\mathbf{r}s) (\nabla_\alpha v_{\mu\mathbf{k}}^{*(q)}(\mathbf{r}s')) \right] [\sigma_\beta]_{ss'},\end{aligned}\quad (40)$$

where  $\alpha$  and  $\beta$  in Eq. (40) are spatial indexes,  $\alpha, \beta = x, y, z$ . In case of the slab phase, the dimensionless Bloch wave functions depend only on  $z$  coordinate perpendicular to the slabs, *i.e.*  $\tilde{u}_{\mu\mathbf{k}}^{(q)}(z\sigma)$  and  $\tilde{v}_{\mu\mathbf{k}}^{(q)}(z\sigma)$  [15], which enables us to significantly reduce the computational cost. For more specific representations of densities and potentials for the slab phase, we refer the readers to Ref. [14, 15].

### C. Finite-temperature extension

Next, let us introduce the finite-temperature extension of the superfluid band theory. We start from the grand canonical ensemble, where the thermodynamic equilibrium is represented as

$$\delta\Omega = 0,\quad (41)$$

where the grand potential  $\Omega$  is given by

$$\Omega = E - TS - \lambda N.\quad (42)$$

In accordance with the equilibrium condition, the expectation value of physical quantities can be obtained with the following operator:

$$\hat{D} = \frac{1}{Z} e^{-\beta(\hat{H} - \lambda\hat{N})},\quad (43)$$



where  $\beta = 1/k_B T$  is the inverse temperature with the Boltzmann constant  $k_B$  and  $\mathcal{Z}$  denotes the partition function,  $\mathcal{Z} = \text{Tr} \left[ e^{-\beta(\hat{H} - \lambda \hat{N})} \right]$ .

Applying the operator  $\hat{D}$  to the HFB theory, we can obtain the representations of the density matrix and the pairing tensor, respectively, as

$$\rho = V^*(1 - f)V^T + UfU^\dagger, \quad (44)$$

$$\kappa = V^*(1 - f)U^T + UfV^\dagger, \quad (45)$$

where the matrix  $f$  is composed of matrix elements  $f_{\mu\nu} = f_\beta(E_\mu)\delta_{\mu\nu}$  with  $f_\beta(E)$  the Fermi-Dirac distribution function,

$$f_\beta(E) = \frac{1}{1 + e^{\beta E}}. \quad (46)$$

As a consequence, various densities are replaced by mixture of contributions from  $u$ - and  $v$ -components of the quasiparticle wave functions. In general, we define the matrix vector  $\rho = [\rho, \tau, \dots]$  and the calculation formula for each element as

$$\rho = \sum_{\mu k \sigma} \mathcal{F}[v_{\mu k \sigma}^{(q)}], \quad (47)$$

where  $\mathcal{F} = [\mathcal{F}_\rho, \mathcal{F}_\tau, \dots]$  is a shorthand notation which, for instance, works as  $\mathcal{F}_\rho[X] = |X|^2$  for the number density,  $\mathcal{F}_\tau[X] = |\nabla X|^2$  for the kinetic energy density and similar for the others. Using this definition, densities other than the anomalous density in the finite temperature system can be written as

$$\rho(\mathbf{r}, T) = \sum_{\mu k \sigma} \left\{ f_\beta(E_{\mu k}) \mathcal{F}[u_{\mu k \sigma}^{(q)}] + f_\beta(-E_{\mu k}) \mathcal{F}[v_{\mu k \sigma}^{(q)}] \right\}, \quad (48)$$

and the anomalous density is given by

$$\kappa_q(\mathbf{r}) = \sum_{\mu k} [f_\beta(-E_{\mu k}) - f_\beta(E_{\mu k})] v_{\mu k \uparrow}^{(q)*}(\mathbf{r} \sigma) u_{\mu k \downarrow}^{(q)}(\mathbf{r} \sigma). \quad (49)$$

For a finite temperature system, an equilibrium solution is obtained by minimizing the Helmholtz's energy,

$$F = E - TS, \quad (50)$$

where the one-particle entropy  $S$  is given by

$$S = -k_B \sum_{\mu} \left[ f_\beta(E_\mu) \ln f_\beta(E_\mu) + [1 - f_\beta(E_\mu)] \ln [1 - f_\beta(E_\mu)] \right]. \quad (51)$$

Since we can calculate the total energy as a function of temperature, the specific heat can be directly calculated as

$$C_V(T) = \frac{\partial E(T)}{\partial T}. \quad (52)$$

We will use the specific heat to characterize phase transitions.

## D. Extension for systems under a magnetic field

In this section, we describe how to introduce a magnetic field  $\mathbf{B}$  into the superfluid band theory at arbitrary temperature  $T$ . There are two major modifications: the first one is modification of single-particle energies through the coupling between nucleonic magnetic moments and  $\mathbf{B}$ ; the second one is modification of electrons' energies because of the Landau-Rabi quantization.

The modification of the nuclear part can be achieved by introducing an additional term to the single-particle Hamiltonian as

$$\hat{h}_{q, \sigma \sigma'} = \hat{h}_{q, \sigma \sigma'}^{(0)} + \hat{h}_{q, \sigma \sigma'}^{(B)}, \quad (53)$$

where  $\hat{h}_{q, \sigma \sigma'}^{(0)}$  denotes the original single-particle Hamiltonian without magnetic field. The second term,  $\hat{h}_{q, \sigma \sigma'}^{(B)}$ , which represents the magnetic effects, is given by

$$\hat{h}_{q, \sigma \sigma'}^{(B)} = - \left( l \delta_{q, p} + g_q \frac{\boldsymbol{\sigma}}{2} \right) \cdot \tilde{\mathbf{B}}_q, \quad (54)$$

where  $l$  is the dimensionless orbital angular momentum (*i.e.*  $\mathbf{L} = \hbar \mathbf{l}$ ),  $\boldsymbol{\sigma}$  is the Pauli matrices, and  $\tilde{\mathbf{B}}_q = (e\hbar/2m_q c) \mathbf{B}$ . Here,  $g_q$  is the g-factors of neutrons and protons, which are given by

$$g_n = -3.826, \quad g_p = +5.585 \quad (55)$$

The first term in Eq. (54) denotes the orbital contribution which couples only with protons, while the second one represents the coupling with nucleons' intrinsic spin. Note that the first term is absent in the slab phase under study.

It is customary to quantify the magnetic field strength relative to the critical value at which energy of the electron's cyclotron motion reaches their rest mass,

$$B_c = \frac{m_e^2 c^3}{e\hbar} \simeq 4.41 \times 10^{13} \text{ G}, \quad (56)$$

denoting  $B_* \equiv B/B_c$ . Using this notation,  $\tilde{\mathbf{B}}_q$  can be written as

$$\tilde{\mathbf{B}}_q = \frac{m_e^2}{2m_q} \mathbf{B}_*. \quad (57)$$

The energy of Landau levels of relativistic electrons is given by

$$e_\nu = \sqrt{c^2 p_z^2 + m_e^2 c^4 (1 + 2\nu B_*)}, \quad (58)$$

where  $\nu$  is an index of the Landau levels which is a non-negative integer, and  $p_z$  is a momentum along the  $z$  axis parallel to the magnetic field (perpendicular to the slabs). The energies of occupied states should be below the chemical potential,  $e_\nu \leq \mu_e$ , for existing  $p_z > 0$ , which is equivalent to

$$\nu \leq \frac{1}{2B_*} \left( \frac{\mu_e^2}{m_e^2 c^4} - 1 \right). \quad (59)$$

Defining the maximum integer satisfying the above condition as  $\nu_{\max}$ , the electron number density and energy density are written by

$$n_e = \frac{2B_\star}{(2\pi)^2 \lambda_e^3} \sum_{\nu=0}^{\nu_{\max}} g_\nu x_e(\nu), \quad (60)$$

$$\mathcal{E}_e = \frac{B_\star m_e c^2}{(2\pi)^2 \lambda_e^3} \sum_{\nu=0}^{\nu_{\max}} g_\nu (1 + 2\nu B_\star) \psi_+ \left[ \frac{x_e(\nu)}{\sqrt{1 + 2\nu B_\star}} \right] - n_e m_e c^2, \quad (61)$$

with

$$\psi_\pm(x) = x\sqrt{1+x^2} \pm \ln\left(x + \sqrt{1+x^2}\right), \quad (62)$$

$$x_e(\nu) = \sqrt{\gamma_e^2 - 1 - 2\nu B_\star}, \quad (63)$$

$$\gamma_e = \frac{\mu_e}{m_e c^2}, \quad (64)$$

$$\lambda_e = \frac{\hbar}{m_e c}. \quad (65)$$

The chemical potential  $\mu_e$  should be determined in such a way that it obeys the  $\beta$ -equilibrium condition,  $\mu_n = \mu_p + \mu_e$ , and the charge neutrality condition,  $n_e = \frac{1}{a} \int n_p(\mathbf{r}) d\mathbf{r} = N_p/a$ .

Note that the magnetic field breaks the time-reversal symmetry. One should thus introduce the time-odd densities such as  $s_q$ ,  $\mathbf{T}_q$ , and  $\mathbf{j}_q$ . Further, if the external magnetic field is strong enough, one may expect that the nucleons are spin-polarized. To quantify the spin polarization, we define the local spin polarization as

$$p_q(z) = \frac{n_{q,\uparrow}(z) - n_{q,\downarrow}(z)}{n_{q,\uparrow}(z) + n_{q,\downarrow}(z)} = \frac{s_{z,q}(z)}{n_q(z)}, \quad (66)$$

where in the last expression we use the  $z$  component of the time-odd spin density,  $s_{z,q}(z)$ . We also define the total spin polarization of the system,

$$P_q = \frac{N_{q,\uparrow} - N_{q,\downarrow}}{N_{q,\uparrow} + N_{q,\downarrow}}, \quad (67)$$

where  $N_{q,\sigma} = \int n_{q,\sigma}(\mathbf{r}) d\mathbf{r}$ . Without the magnetic field, the system is unpolarized and at certain critical magnetic field strength one should observe spin polarization as a sort of phase transition.

### III. RESULTS AND DISCUSSION

#### A. Computational Settings

We use our own computational code for self-consistent superfluid band theory calculations and employ the same computational settings as in our previous work [15], such as the discretization numbers, otherwise specified. All the calculations have been performed under the  $\beta$ -equilibrium condition. Ideally, one should determine an optimal slab period by minimizing the total energy of the system with respect to

the distance between neighboring slabs (slab period), which we denote as  $a$ . However, we find that the optimal slab period  $a$ , which provides the minimum energy of the system, is somewhat ambiguous to determine. Furthermore, it has been pointed out in Ref. [16] that the optimal cell size significantly depends on the choice of the energy density functionals. Since our main purpose of the present work is to investigate qualitative features of finite-temperature and magnetic fields effects, and they may also influence the optimal slab period, the period length is fixed to  $a = 30$  fm or  $a = 40$  fm, for simplicity. For comparison among various densities, we set  $n_B = 0.04, 0.05, 0.06,$  and  $0.07$  fm $^{-3}$ , as in our previous work [15].

We note here that the band structure effects provide only minor corrections to the results discussed in the present paper. Thus, in the following, we focus on the effects of superfluidity, finite temperature and magnetic field, although all the results shown below include the band structure effects.

#### B. Finite-temperature effects

In this section, we restrict the analysis to the  $B = 0$  case (without magnetic field), focusing on how the properties of nuclear matter are affected by finite-temperature effects. We will investigate effects of finite magnetic field in the next section.

##### 1. Pairing and structural phase transitions

Figure 1 shows spatial distributions of the nucleon number densities [Fig. 1(a)] and pairing fields [Fig. 1(b)] as a function of  $z$  coordinate, for several representative temperatures. The baryon number density and the slab period are fixed to  $n_B = 0.05$  fm $^{-3}$  and  $a = 30$  fm, respectively. In Fig. 1(a), the results obtained for  $k_B T = 0, 1, 3, 4,$  and  $5$  MeV are shown, while in Fig. 1(b) those for  $k_B T = 0, 0.3, 0.5,$  and  $0.8$  MeV are shown. In ascending order with those temperatures, solid, dashed, dotted, dash-dotted, and long-dashed lines are used. In both cases, green lines exhibiting larger values correspond to neutrons' contribution, while red lines exhibiting smaller values correspond to protons' ones.

From Fig. 1(a), we find that the density distributions are almost unchanged up to  $k_B T = 1$  MeV. As the temperature increases further, the slab shape becomes gradually diffusive at  $k_B T = 3$  MeV (dotted lines) and 4 MeV (dash-dotted line), and finally the slab completely melts at  $k_B T = 5$  MeV (long-dashed lines) being a uniform nuclear matter for both neutrons and protons. In contrast, from Fig. 1(b), we find that the pairing field strength depends sensitively on temperature. Already at  $k_B T = 0.3$  MeV, the proton pairing field vanishes, whereas neutron's one sustains a sizable value. As the temperature increases further, the neutron pairing field vanishes as well at  $k_B T = 0.8$  MeV.

These results indicate that two kinds of phase transitions occur in nuclear matter as the temperature increases: 1) the pairing phase transition of neutrons (protons) from superfluid

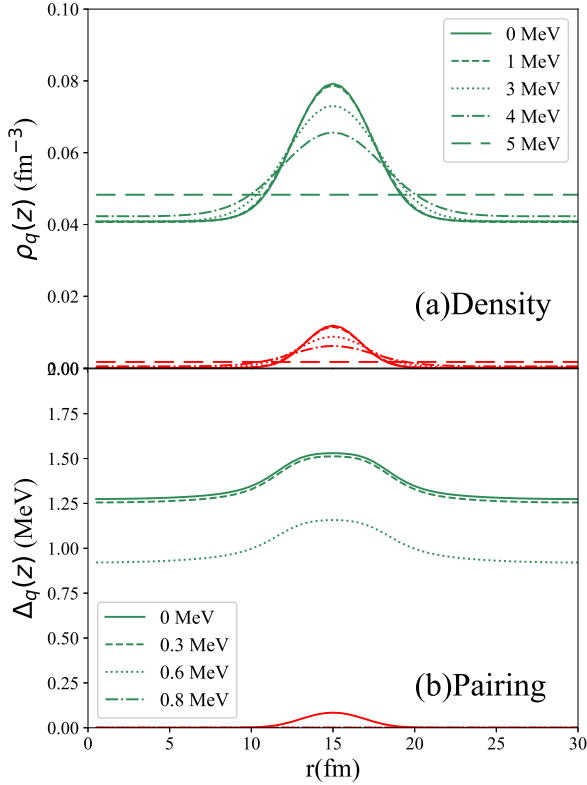


FIG. 1. (a) Density distributions and (b) pairing fields of neutrons and protons are shown as a function of  $z$  coordinate at four representative temperatures,  $k_B T = 0, 1, 3, 4,$  and  $5$  MeV. In both panels, the upper green lines indicate the distribution of neutrons' quantities, while the red lines are that for protons' ones. In ascending order of temperatures, solid, dashed, dotted, dash-dotted, and long-dashed lines are used.

(superconducting) to the normal phase, and 2) the structural transition from nuclear pasta to uniform matter.

## 2. Heat capacity and critical temperatures

The critical temperature of the phase transitions can be determined more precisely by analyzing the specific heat (52). To calculate the specific heat, we perform finite-temperature calculations by changing temperature with  $k_B \Delta T = 0.01$ -MeV step and evaluate the first derivative of the total energy with 9-points formula. We have confirmed that the results are not sensitive to a change of the order of the finite-difference method. In Figs. 2(a) and 2(b), the total energy and specific heat are exhibited, respectively, which are calculated for a fixed slab period  $a = 30$  fm. In Fig. 2(a), we show the total energy for a representative baryon number density,  $n_B = 0.04 \text{ fm}^{-3}$ , while the specific heat is shown in Fig. 2(b), for a range of baryon number densities,  $n_B = 0.04, 0.05, 0.06,$  and  $0.07 \text{ fm}^{-3}$ . From Fig. 2(a), we find a continuous, yet non-smooth behavior of the total energy curve as a function of temperature, at around  $k_B T = 0.7$  and  $4.5$  MeV (represented by black arrows), indicating second-order phase transi-

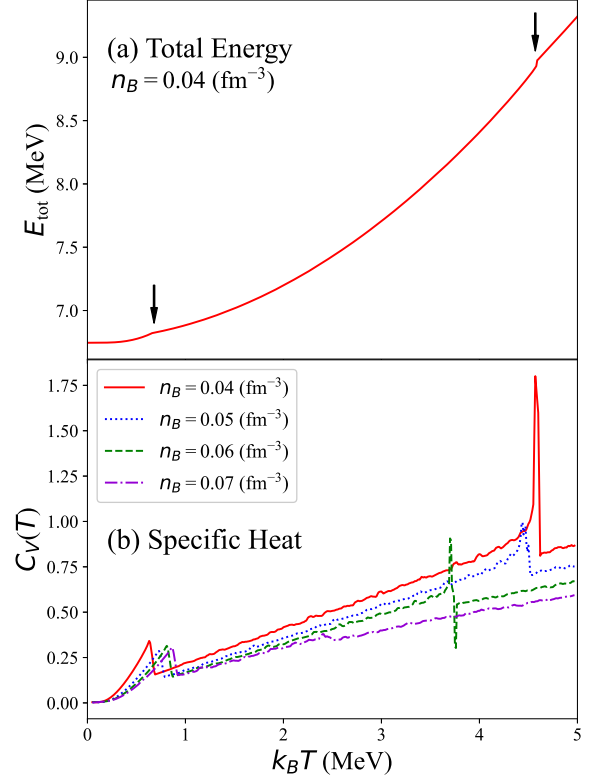


FIG. 2. (a) Total energy per nucleon,  $E_{\text{tot}}$ , is shown as a function of temperature for a fixed baryon density,  $n_B = 0.04 \text{ fm}^{-3}$ . Two arrows indicate the position of kinks implying phase transitions. (b) Specific heat  $C_V(T)$  is shown as a function of temperature, for different baryon number densities,  $n_B = 0.04, 0.05, 0.06,$  and  $0.07 \text{ fm}^{-3}$ . In ascending order of densities, solid, dashed, dotted, and dash-dotted lines are used.

tions. Correspondingly, the specific heat exhibits two sharp kinks at around those temperatures. We define the critical temperature of the phase transition as the local maximum of the specific heat (neglecting small thermal fluctuations). For  $n_B = 0.04 \text{ fm}^{-3}$  (red solid line), the critical temperatures at the two sharp kinks are found to be  $0.63$  and  $4.57$  MeV, respectively. Here and henceforth, let us denote the lower-energy critical temperature for the superfluid phase transition as  $T_c^{\text{sf}}$  and the higher-energy critical temperature for the structural phase transition (melting temperature) as  $T_c^{\text{melt}}$ . As the baryon number density increases, we find that  $T_c^{\text{sf}}$  slightly shifts towards higher temperatures, while  $T_c^{\text{melt}}$  shows the opposite trend, which decreases with increasing baryon number density.

In Table I, we summarize the critical temperatures obtained for the baryon number densities examined for the two slab periods,  $a = 30$  and  $40$  fm. The critical temperature is defined by the peak position of each kink. In the table, the observed shifts are evident: as the baryon number density increases, the critical temperature for the pairing phase transition ( $T_c^{\text{sf}}$ ) increases, while that for the structural phase transition ( $T_c^{\text{melt}}$ ) decreases, regardless of the slab period  $a$ . The observed tendency can be explained as follows. The increase in baryon



TABLE I. Calculated critical temperatures for the superfluid phase transition,  $T_c^{\text{sf}}$ , and the structural transition,  $T_c^{\text{melt}}$ , are listed in units of MeV, for a couple of baryon number densities,  $n_B = 0.04, 0.05, 0.06,$  and  $0.07 \text{ fm}^{-3}$ , and the two slab periods,  $a = 30$  and  $40 \text{ fm}$ .

$n_B \text{ (fm}^{-3}\text{)}$	0.04	0.05	0.06	0.07
$T_c^{\text{sf}}(a = 30) \text{ (MeV)}$	0.63	0.73	0.81	0.86
$T_c^{\text{melt}}(a = 30) \text{ (MeV)}$	4.57	4.32	3.70	2.40
$T_c^{\text{sf}}(a = 40) \text{ (MeV)}$	0.65	0.75	0.83	0.89
$T_c^{\text{melt}}(a = 40) \text{ (MeV)}$	4.82	4.44	3.44	2.75

number density implies that the number of nucleons at each spatial point increases, which necessitates greater thermal perturbations to disrupt the pairing interactions. Conversely, as the baryon number density increases, the density distribution becomes more diffusive and approaches that of uniform nuclear matter [*cf.* Fig. 1(a)], leading to a lower critical temperature for the structural phase transition. In this way, the temperature dependence of nuclear matter properties varies with the baryon number density. We point out here that the critical temperatures do not depend much on the slab period  $a$ , justifying our fixed- $a$  treatment in the present study.

### C. Magnetic field effects

In this section, we investigate the influence of external magnetic field on the properties of nuclear matter. We will show the results at both zero and finite temperatures to examine an interplay of effects of finite temperature and magnetic field.

#### 1. Pairing phase transition

In Fig. 3(a), we show the average magnitude of the neutron pairing field,  $\overline{\Delta}_n = \int \Delta_n(z) n_n(z) dz / N_n$ , for the case of  $n_B = 0.05 \text{ fm}^{-3}$  and  $a = 30 \text{ fm}$ , as a function of the magnetic-field strength at four representative temperatures. In the figure, the results obtained for  $k_B T = 0, 10, 100,$  and  $1000 \text{ keV}$  are shown by solid, dashed, dotted, and dash-dotted lines with circle, upward triangle, downward triangle, and rectangular symbols, respectively.

From Fig. 3(a), we find that the average neutron pairing gap remains nearly constant as a function of the magnetic field strength, up to a certain critical value, beyond which it steeply drops down to zero, meaning that the Cooper pairs are broken by the magnetic field. Note that since  $T_c^{\text{sf}} = 0.73 \text{ MeV}$  neutron superfluidity has already disappeared in the  $T = 1000 \text{ keV}$  case even without the magnetic field. Although this behavior seems to be a first-order phase transition, the existence of an intermediate regime within a narrow magnetic field window suggests that it is more appropriately classified as a second-order phase transition. The critical magnetic field strength for the Cooper-pair breaking decreases as the temperature increases, while the transition to the normal phase occurs more gradually at finite temperatures as compared to the zero-

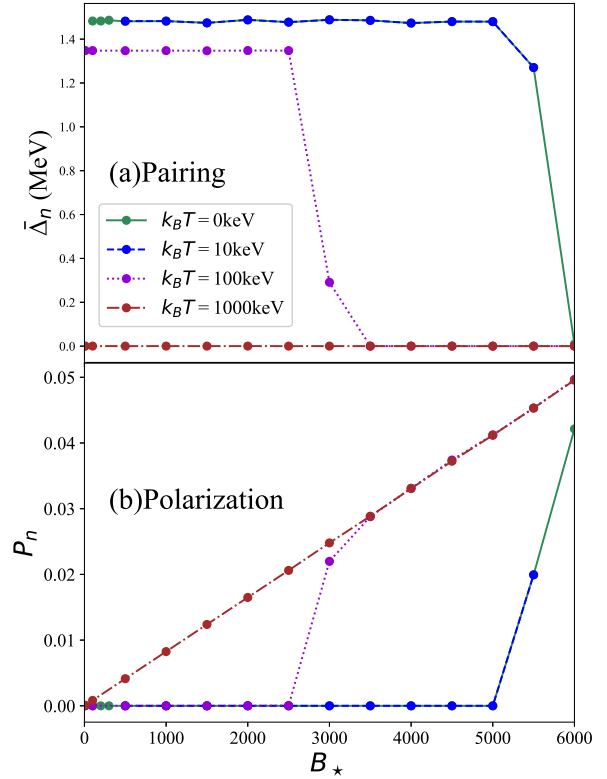


FIG. 3. (a) Average magnitude of the neutron pairing field,  $\overline{\Delta}_n$ , and (b) total spin polarization,  $P_n$ , of neutrons are shown as a function of the magnetic field strength,  $B_*$ , at four representative temperatures,  $k_B T = 0, 10, 100,$  and  $1000 \text{ keV}$ . In ascending order of temperatures, circle, upward triangle, downward triangle, and rectangular symbols connected with solid, dashed, dotted, and dash-dotted lines are used, respectively.

temperature case. In this way, the superfluid to normal phase transition occurs suddenly at a certain critical magnetic field strength, indicating an onset of spin polarization.

#### 2. Spin polarization

In the inner crust of neutron stars, neutrons are in a superfluid phase associate with spin-singlet  $s$ -wave ( $^1S_0$ ) pairing interaction. On the other hand, the coupling with the external magnetic field would prefer nucleons' spin to be parallel to the magnetic field (*i.e.* spins are polarized). There is thus apparent competition between nuclear pairing and magnetic-field interactions. By incorporating the magnetic-field coupling into the finite-temperature SLDA formalism, we can now investigate the competition between nuclear pairing correlations and the magnetic field effects in a fully microscopic manner.

In Fig. 3(b), the total spin polarization of neutrons,  $P_n = (N_{n,\uparrow} - N_{n,\downarrow}) / (N_{n,\uparrow} + N_{n,\downarrow})$ , is shown as a function of the magnetic field strength,  $B_*$ . Four lines and symbols correspond to four representative temperatures in the same way as Fig. 3(a). From the figure, we find that the system remains unpolarized ( $P_n = 0$ ) up to a certain critical magnetic field

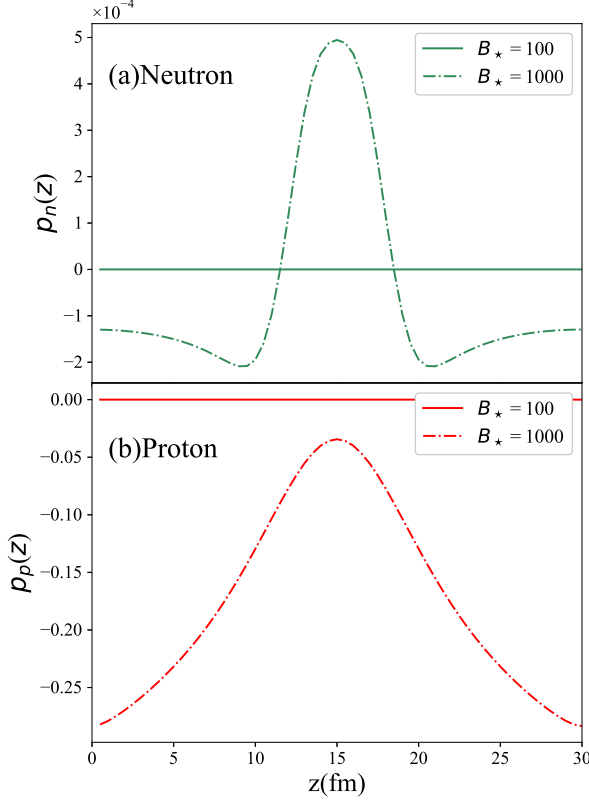


FIG. 4. Distributions of the local spin polarization of neutrons,  $p_n(z)$ , and protons,  $p_p(z)$ , are shown in panels (a) and (b), respectively, as a function of  $z$  coordinate for two magnetic field strengths,  $B_* = 100$  and 1000. Results for  $B_* = 100$  are shown by solid lines, while those for  $B_* = 1000$  are shown by dashed lines.

strength. (We note that protons are already polarized even at small magnetic field about  $B_* \approx 200$  due to a small proton pairing gap.) Beyond the critical value, the system abruptly attains small, yet finite polarization. The critical value coincides with the ones at which we observed sudden drops of the average neutron pairing gap in Fig. 3(a). Following the onset of polarization, both protons and neutrons exhibit an almost linear increase of polarization with increasing the magnetic field strength. In the figure, it is evident that the critical magnetic field for the onset of spin polarization decreases substantially as the temperature increases. Eventually, at the temperature of  $k_B T = 1$  MeV, the pairing vanishes even without the magnetic field, and polarization increases linearly with the magnetic field strength. Because of the clear correlation of the changes in the average neutron pairing gap and the spin polarization, we can expect that there exists an interplay between nucleon pairing and spin polarization.

Let us now look in more detail internal structure of the system under external magnetic field. In Figs. 4(a) and 4(b), we show the local polarization of neutrons and protons, respectively, as a function of  $z$  coordinate at  $B_* = 100$  and 1000 and  $T = 0$ . As indicated in Fig. 3, the  $B_* = 100$  case corresponds

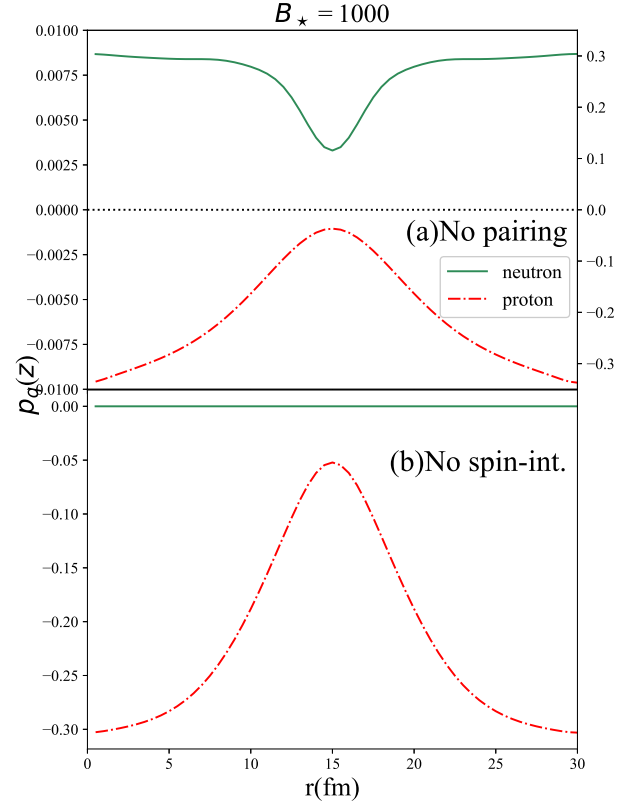


FIG. 5. Distributions of the local spin polarization of neutrons (green solid lines) and of protons (red dash-dotted lines) are shown as a function of  $z$  coordinate for the  $B_* = 1000$  case. In panel (a), results without the pairing interaction are presented, while in panel (b) results without the spin-dependent interaction are shown.

to the paramagnetic phases for both protons and neutrons, and with  $B_* = 1000$  only protons are polarized. From Figs. 4(a) and 4(b), it is more evident that both neutrons and protons are not polarized at all for all spatial points (*i.e.*  $p_q(z) = 0$ ) in the  $B_* = 100$  case (solid line). On the other hand, by looking at the  $B_* = 1000$  case, we find several intriguing properties of the nuclear matter under an external magnetic field: 1) in the central region where the nuclear slab resides, protons and neutrons are polarized in opposite directions (*i.e.*  $p_n > 0$  and  $p_p < 0$ ), because of the opposite signs of the nucleons'  $g$ -factor. On the contrary, looking at the region of dripped neutrons outside the slab, we find that both neutrons and protons are locally polarized along the same direction (*i.e.*  $p_n < 0$  and  $p_p < 0$ ), that is, the local polarization of neutrons changes its sign. It must be emphasized that neutrons are not polarized in total even at  $B_* = 1000$ , as shown in Fig. 3.

To understand the observed local spin polarization of neutrons at  $B_* = 1000$ , we performed additional calculations with two different interaction setups. In Fig. 5(a), we show the local spin polarization for the  $B_* = 1000$  case, switching off the pairing interaction (*i.e.*  $\Delta_q = 0$ ). By comparing Figs. 4(a) (dash-dotted line) and 5(a) (solid line), we find a

qualitative change of the local spin polarization of neutrons at  $B_\star = 1000$ . That is, without the pairing interaction, neutrons get spin polarized in total, and the distribution of  $p_n(z)$  becomes somewhat similar to  $p_p(z)$  with an opposite sign. Additionally, we show in Fig. 5(b) the same quantities as in Fig. 5(a), but with the pairing interaction and without spin-dependent interactions, for comparison. In the latter case, we omit terms that contain time-odd spin densities ( $s_q$ ) in the EDF. In stark contrast, we find that neutrons are completely unpolarized in whole space ( $p_n(z) = 0$ ), simply because spin-singlet Cooper pairs are preserved. From these observations, we conclude that the locally polarized system in the presence of pairing is realized as a result of an interplay between pairing and spin-dependent interactions. On the one hand, the spin-singlet pairing interaction prefers to hold the system unpolarized in total, on the other hand, the spin-dependent interactions prefer to reduce the isoscalar spin density ( $s_{z,0} = s_{z,n} + s_{z,p}$ ), assisting neutrons and protons to be polarized in opposite directions. We note here that the latter effects depend on time-odd terms in the EDF that contain  $C_t^s$ ,  $C_{td}^s$ ,  $C_t^T$  coefficients, which are less constrained as compared to time-even terms. It is thus worthwhile to explore functional dependence of the role of spin-dependent terms, which we leave for a future work.

To summarize, our superfluid band theory calculations indicate that, even below the critical magnetic field strength at which Cooper pairs are broken, neutrons inside and outside the cluster can be polarized in the opposite directions to each other, maintaining zero total polarization of the system. It is interesting to note that the observed local polarization keeping  $\Delta$  unchanged implies that neutrons still form Cooper pairs, where one locates inside and the other locates outside of nuclear clusters. Note that  $B_\star = 1000$  corresponds to  $B \sim 4.41 \times 10^{16}$  G that might be realized in magnetars. In such situations, some phenomena may be affected by the local polarizations inside and outside of the cluster in the inner crust of neutron stars.

#### IV. SUMMARY AND PROSPECT

In this work, we have extended the formalism of the fully-microscopic superfluid band theory based on the Kohn-Sham density functional theory (DFT) for superfluid systems, known as superfluid local density approximation (SLDA), to take into account effects of finite temperature and magnetic field. For finite-temperature systems, densities are calculated with a mixture of  $u$ - and  $v$ -components of quasiparticle wave functions, in the way familiar with the finite-temperature Hartree-Fock-Bogoliubov theory. For finite-magnetic field systems, the chemical potential of relativistic electrons is calculated with the Landau-Rabi quantization taken into account, which affects the composition of neutrons and protons through the  $\beta$ -equilibrium condition. Furthermore, the effect of magnetic field on nucleons is incorporated by introducing the coupling between an external magnetic field and nucleons' magnetic moment to the single-particle Hamiltonian. The framework developed in this way enables us fully-

microscopic calculations for neutron star matter under realistic conditions of temperature and magnetic field. In this work, we have demonstrated its feasibility by applying it to the slab phase of nuclear matter.

From the results of finite-temperature calculations, we have found that there appear two kinds of phase transitions: one is the pairing phase transition at around  $k_B T = 1$  MeV for neutrons, and the other is the structural transition (*i.e.* melting of clusters) at around  $k_B T = 4$  MeV. In addition, we have found that the critical temperatures exhibit systematic dependence on the baryon number density. That is, as the baryon number density increases, the critical temperature for the pairing (structural) phase transition increases (decreases). The former indicates stronger pairing interactions among neutrons at a certain position, while the latter reflects shape changes of the cluster which becomes more diffusive (approaching uniform nuclear matter) at higher baryon number densities.

From the results of finite magnetic-field calculations, we have demonstrated a rich character of phases of the inner crust of neutron stars under an external magnetic field. Up to certain critical magnetic field strength, neutrons preserve  $^1S_0$  superfluidity which hinders neutron spin polarization. This critical temperature decreases as the temperature increases due to thermal disturbance to pairing, which may be recognized as an anti-ferromagnetic behavior. At larger magnetic field strength beyond the critical value,  $^1S_0$  Cooper pairs are broken and the neutrons' spin polarization increases linearly with the magnetic field strength, which behaves like a paramagnetic matter. From a detailed analysis of spatial distribution of local spin polarization, we have found that neutrons inside and outside the cluster are polarized locally even below the critical magnetic field strength. Namely, neutrons inside the cluster are polarized opposite to the spin polarization of protons, as expected from the different signs of the nuclear  $g$ -factor of neutrons and protons. Intriguingly, neutrons outside the cluster are actually polarized in the opposite direction parallel to that of protons, thereby keeping the total spin polarization of neutrons in the system zero. It means that neutrons inside the cluster exhibit paramagnetic behavior, whereas dripped neutrons behaves as if they have a diamagnetic property. We have demonstrated that the observed local spin polarization can be understood as an interplay between pairing and spin-dependent interactions. Although the spin polarization occurs abruptly like a first-order phase transition at zero temperature, it becomes moderate at finite temperature. These findings may provide potential impact on physics of neutron stars under realistic astrophysical conditions where effects of finite temperature and magnetic field are not negligible, such as cooling processes of a proto-neutron star [63].

As a future work, we plan to extend our theoretical framework to two- and three-dimensional geometries. By extending the present formalism for those higher dimensions, it will be the most sophisticated theory to describe neutron star matter, taking into account effects of finite temperature and magnetic field, as well as superfluidity and band structure effects on the same footing, in a fully self-consistent manner. In the outer core of neutron stars, neutrons are expected to form the spin-triplet  $p$ -wave ( $^3P_2$ ) superfluid, which may be resistive against

an external magnetic field and, thus, it may alter the behavior of the spin polarization. It is possible to extend the formalism to account for the  $^3P_2$  pairing by introducing the spin-current pair density as discussed in Ref. [64]. In one-dimensional systems, the absence of spin-orbit interactions precludes the emergence of such spin-triplet pairing; however, in systems of two dimensions or higher, these correlations are expected to play a pivotal role. Furthermore, in the context of cold-atom physics, it has been discussed that, spin polarization induces a variety of phases such as Larkin-Ovchinnikov-Fulde-Ferrell (LOFF) phase [49–51] or a spin-polarized droplet called *ferro* [52, 53] and its complex patterns [54]. It would also be interesting to explore possible topological structures in nuclear matter such as Skermin crystal [65, 66]. Taking into account all these internal and external effects, we will be able to establish the comprehensive microscopic framework for investigating the properties of neutron star matter in realistic astrophysical conditions, from the birth to later years in the life cycle of

neutron stars.

## ACKNOWLEDGMENTS

We would like to thank Kenichi Yoshida (RCNP, Osaka University) and Takashi Nakatsukasa (University of Tsukuba) for valuable discussions. One of the authors (K.Y.) appreciate the support from the Hiki Foundation, Institute of Science Tokyo. This work is supported by the JSPS Research Fellow, Grant No. 24KJ1110, as well as JSPS Grant-in-Aid for Scientific Research, Grants No. 23K03410 and No. 23K25864. This work mainly used computational resources of the Yukawa-21 supercomputer at Yukawa Institute for Theoretical Physics (YITP), Kyoto University. This work also used (in part) the computational resources of TSUB-AME4.0 at Institute of Science Tokyo, through the HPCI System Project, Project ID: hp230180 and hp240183.

- 
- [1] P. Hohenberg and W. Kohn, Inhomogeneous Electron Gas, *Phys. Rev.* **136**, B864 (1964).
- [2] W. Kohn and L. J. Sham, Self-Consistent Equations Including Exchange and Correlation Effects, *Phys. Rev.* **140**, A1133 (1965).
- [3] T. Nakatsukasa, K. Matsuyanagi, M. Matsuo, and K. Yabana, Time-dependent density-functional description of nuclear dynamics, *Rev. Mod. Phys.* **88**, 045004 (2016).
- [4] G. Colò, Nuclear density functional theory, *Advances in Physics: X* **5**, 1740061 (2020).
- [5] M. Bender, P.-H. Heenen, and P.-G. Reinhard, Self-consistent mean-field models for nuclear structure, *Rev. Mod. Phys.* **75**, 121 (2003).
- [6] B. Schuetrumpf and W. Nazarewicz, Twist-averaged boundary conditions for nuclear pasta hartree-fock calculations, *Phys. Rev. C* **92**, 045806 (2015).
- [7] F. J. Fattoyev, C. J. Horowitz, and B. Schuetrumpf, Quantum nuclear pasta and nuclear symmetry energy, *Phys. Rev. C* **95**, 055804 (2017).
- [8] B. Schuetrumpf, G. Martínez-Pinedo, M. Afibuzaman, and H. M. Aktulga, Survey of nuclear pasta in the intermediate-density regime: Shapes and energies, *Phys. Rev. C* **100**, 045806 (2019).
- [9] B. Schuetrumpf, G. Martínez-Pinedo, and P.-G. Reinhard, Survey of nuclear pasta in the intermediate-density regime: Structure functions for neutrino scattering, *Phys. Rev. C* **101**, 055804 (2020).
- [10] B. Schuetrumpf, M. A. Klatt, K. Iida, J. A. Maruhn, K. Mecke, and P.-G. Reinhard, Time-dependent hartree-fock approach to nuclear “pasta” at finite temperature, *Phys. Rev. C* **87**, 055805 (2013).
- [11] B. Schuetrumpf, K. Iida, J. A. Maruhn, and P.-G. Reinhard, Nuclear “pasta matter” for different proton fractions, *Phys. Rev. C* **90**, 055802 (2014).
- [12] B. Schuetrumpf, M. A. Klatt, K. Iida, G. E. Schröder-Turk, J. A. Maruhn, K. Mecke, and P.-G. Reinhard, Appearance of the single gyroid network phase in “nuclear pasta” matter, *Phys. Rev. C* **91**, 025801 (2015).
- [13] Y. Kashiwaba and T. Nakatsukasa, Self-consistent band calculation of the slab phase in the neutron-star crust, *Phys. Rev. C* **100**, 035804 (2019).
- [14] K. Sekizawa, S. Kobayashi, and M. Matsuo, Time-dependent extension of the self-consistent band theory for neutron star matter: Anti-entrainment effects in the slab phase, *Phys. Rev. C* **105**, 045807 (2022).
- [15] K. Yoshimura and K. Sekizawa, Superfluid extension of the self-consistent time-dependent band theory for neutron star matter: Anti-entrainment versus superfluid effects in the slab phase, *Phys. Rev. C* **109**, 065804 (2024).
- [16] G. Almirante and M. Urban, Superfluid fraction in the slab phase of the inner crust of neutron stars, *Phys. Rev. C* **109**, 045805 (2024).
- [17] G. Almirante and M. Urban, Superfluid fraction in the rod phase of the inner crust of neutron stars, *Phys. Rev. C* **110**, 065802 (2024).
- [18] N. W. Ashcroft and N. D. Mermin, *Solid state physics* (Holt, Rinehart and Winston, New York, NY, 1976).
- [19] B. Carter, N. Chamel, and P. Haensel, Entrainment coefficient and effective mass for conduction neutrons in neutron star crust: Simple microscopic models, *Nuclear Physics A* **748**, 675 (2005).
- [20] N. Chamel, Band structure effects for dripped neutrons in neutron star crust, *Nuclear Physics A* **747**, 109 (2005).
- [21] N. Chamel, R. L. Pavlov, L. M. Mihailov, Ch. J. Velchev, Zh. K. Stoyanov, Y. D. Mutafchieva, M. D. Ivanovich, J. M. Pearson, and S. Goriely, Properties of the outer crust of strongly magnetized neutron stars from Hartree-Fock-Bogoliubov atomic mass models, *Phys. Rev. C* **86**, 055804 (2012).
- [22] N. Chamel, Entrainment in Superfluid Neutron-Star Crusts: Hydrodynamic Description and Microscopic Origin, *J Low Temp Phys* **189**, 328 (2017).
- [23] N. Andersson, K. Glampedakis, W. C. G. Ho, and C. M. Espinoza, Pulsar Glitches: The Crust is not Enough, *Phys. Rev. Lett.* **109**, 241103 (2012).
- [24] N. Chamel, Crustal Entrainment and Pulsar Glitches, *Phys. Rev. Lett.* **110**, 011101 (2013).
- [25] B. Haskell and A. Melatos, Models of pulsar glitches, *Int. J. Mod. Phys. D* **24**, 1530008 (2015).
- [26] A. Y. Potekhin, J. A. Pons, and D. Page, Neutron Stars—Cooling and Transport, *Space Sci Rev* **191**, 239 (2015).



- [27] N. Chamel, D. Page, and S. Reddy, Low-energy collective excitations in the neutron star inner crust, *Phys. Rev. C* **87**, 035803 (2013).
- [28] D. A. Baiko, P. Haensel, and D. G. Yakovlev, Thermal conductivity of neutrons in neutron star cores, *A&A* **374**, 151 (2001).
- [29] E. Flowers and N. Itoh, Transport properties of dense matter, *The Astrophysical Journal* **206**, 218 (1976).
- [30] E. Flowers, M. Ruderman, and P. Sutherland, Neutrino pair emission from finite-temperature neutron superfluid and the cooling of young neutron stars, *The Astrophysical Journal* **205**, 541 (1976).
- [31] D. N. Voskresensky and A. V. Senatorov, Description of Nuclear Interaction in Keldysh's Diagram Technique and Neutrino Luminosity of Neutron Stars. (In Russian), *Sov. J. Nucl. Phys.* **45**, 411 (1987).
- [32] L. B. Leinson, Superfluid response and the neutrino emissivity of baryon matter: Fermi-liquid effects, *Phys. Rev. C* **79**, 045502 (2009).
- [33] L. B. Leinson, Neutrino emission from triplet pairing of neutrons in neutron stars, *Phys. Rev. C* **81**, 025501 (2010).
- [34] K. Makishima, T. Enoto, J. S. Hiraga, T. Nakano, K. Nakazawa, S. Sakurai, M. Sasano, and H. Murakami, Possible Evidence for Free Precession of a Strongly Magnetized Neutron Star in the Magnetar 4U 0142+61\$, *Phys. Rev. Lett.* **112**, 171102 (2014).
- [35] R. Turolla, S. Zane, and A. L. Watts, Magnetars: The physics behind observations. A review, *Rep. Prog. Phys.* **78**, 116901 (2015).
- [36] V. M. Kaspi and A. M. Beloborodov, Magnetars, *Annu. Rev. Astron. Astrophys.* **55**, 261 (2017).
- [37] P. Esposito, N. Rea, and G. L. Israel, Magnetars: A Short Review and Some Sparse Considerations, in *Timing Neutron Stars: Pulsations, Oscillations and Explosions*, edited by T. M. Belloni, M. Méndez, and C. Zhang (Springer, Berlin, Heidelberg, 2021) pp. 97–142.
- [38] D. Peña Artega, M. Grasso, E. Khan, and P. Ring, Nuclear structure in strong magnetic fields: Nuclei in the crust of a magnetar, *Phys. Rev. C* **84**, 045806 (2011).
- [39] D. Basilio, D. P. Artega, X. Roca-Maza, and G. Colò, Outer crust of a cold non-accreting magnetar, *Phys. Rev. C* **92**, 035802 (2015).
- [40] V. Parmar, H. C. Das, M. K. Sharma, and S. K. Patra, Magnetized neutron star crust within effective relativistic mean-field model, *Phys. Rev. D* **107**, 043022 (2023).
- [41] K. Sekizawa and K. Kaba, Possible existence of extremely neutron-rich superheavy nuclei in neutron star crusts under a superstrong magnetic field, arXiv:2302.07923 [nucl-th] (2023).
- [42] A. Bonanno, L. Rezzolla, and V. Urpin, Mean-field dynamo action in protoneutron stars, *A&A* **410**, L33 (2003).
- [43] L. Naso, L. Rezzolla, A. Bonanno, and L. Paternò, Magnetic field amplification in proto-neutron stars: The role of the neutron-finger instability for dynamo excitation, *A&A* **479**, 167 (2008).
- [44] J. Friebe and L. Rezzolla, Equilibrium models of relativistic stars with a toroidal magnetic field, *Monthly Notices of the Royal Astronomical Society* **427**, 3406 (2012).
- [45] M. Stein, J. Maruhn, A. Sedrakian, and P.-G. Reinhard, Carbon-oxygen-neon mass nuclei in superstrong magnetic fields, *Phys. Rev. C* **94**, 035802 (2016).
- [46] W. Jiang and Y.-j. Chen, Role of magnetic fields on the outer crust in a magnetar\*, *Chinese Phys. C* **48**, 074103 (2024).
- [47] D. Basilio, X. Roca-Maza, and G. Colò, Synthesis of super-heavy elements in the outer crust of a magnetar, arXiv:2403.17773 [nucl-th] (2024).
- [48] H. Tajima, H. Funaki, Y. Sekino, N. Yasutake, and M. Matsuo, Exploring  ${}^3p_0$  superfluid in dilute spin-polarized neutron matter, *Phys. Rev. C* **108**, L052802 (2023).
- [49] P. Fulde and R. A. Ferrell, Superconductivity in a Strong Spin-Exchange Field, *Phys. Rev.* **135**, A550 (1964).
- [50] A. I. Larkin and Y. N. Ovchinnikov, Nonuniform state of superconductors, *Zh. Eksp. Teor. Fiz.* **47**, 1136 (1964).
- [51] R. Casalbuoni and G. Nardulli, Inhomogeneous superconductivity in condensed matter and QCD, *Rev. Mod. Phys.* **76**, 263 (2004).
- [52] P. Magierski, B. Tüzemen, and G. Włazłowski, Spin-polarized droplets in the unitary Fermi gas, *Phys. Rev. A* **100**, 033613 (2019).
- [53] P. Magierski, B. Tüzemen, and G. Włazłowski, Dynamics of spin-polarized impurity in ultracold Fermi gas, *Phys. Rev. A* **104**, 033304 (2021).
- [54] B. Tüzemen, T. Zawiślak, G. Włazłowski, and P. Magierski, Disordered structures in ultracold spin-imbalanced Fermi gas, *New J. Phys.* **25**, 033013 (2023).
- [55] A. N. Bogdanov and U. K. Röbber, Chiral Symmetry Breaking in Magnetic Thin Films and Multilayers, *Phys. Rev. Lett.* **87**, 037203 (2001).
- [56] Y. Zhou, E. Iacocca, A. A. Awad, R. K. Dumas, F. C. Zhang, H. B. Braun, and J. Åkerman, Dynamically stabilized magnetic skyrmions, *Nat Commun* **6**, 8193 (2015).
- [57] B. Göbel, I. Mertig, and O. A. Tretiakov, Beyond skyrmions: Review and perspectives of alternative magnetic quasiparticles, *Physics Reports* **895**, 1 (2021), beyond skyrmions: Review and perspectives of alternative magnetic quasiparticles.
- [58] A. Bulgac and Y. Yu, Renormalization of the Hartree-Fock-Bogoliubov Equations in the Case of a Zero Range Pairing Interaction, *Phys. Rev. Lett.* **88**, 042504 (2002).
- [59] A. Bulgac, Local density approximation for systems with pairing correlations, *Phys. Rev. C* **65**, 051305 (2002).
- [60] S. Jin, K. J. Roche, I. Stetcu, I. Abdurrahman, and A. Bulgac, The LISE package: Solvers for static and time-dependent superfluid local density approximation equations in three dimensions, *Computer Physics Communications* **269**, 108130 (2021).
- [61] A. L. Goodman, Finite-temperature HFB theory, *Nuclear Physics A* **352**, 30 (1981).
- [62] T. Duguet and W. Ryssens, Zero-pairing and zero-temperature limits of finite-temperature Hartree-Fock-Bogoliubov theory, *Phys. Rev. C* **102**, 044328 (2020).
- [63] K. Sumiyoshi, S. Furusawa, H. Nagakura, A. Harada, H. Togashi, K. Nakazato, and H. Suzuki, Effects of nuclear matter and composition in core-collapse supernovae and long-term proto-neutron star cooling, *Progress of Theoretical and Experimental Physics* **2023**, 013E02 (2022).
- [64] N. Hinohara, T. Oishi, and K. Yoshida, Triplet-odd pairing in finite nuclear systems: Even-even singly closed nuclei, *Phys. Rev. C* **109**, 034302 (2024).
- [65] S. Hayami, T. Okubo, and Y. Motome, Phase shift in skyrmion crystals, *Nat Commun* **12**, 6927 (2021).
- [66] M.-K. Lee and M. Mochizuki, Reservoir Computing with Spin Waves in a Skyrmion Crystal, *Phys. Rev. Appl.* **18**, 014074 (2022).